

## Supplementary Information (SI) for

# Congruent Permian-Triassic $\delta^{238}\text{U}$ records at Panthalassic and Tethyan sites: confirmation of global-ocean anoxia and validation of the U-isotope paleoredox proxy

Feifei Zhang, Thomas J. Algeo, Stephen J. Romaniello, Ying Cui, Laishi Zhao, Zhong-Qiang Chen, Ariel D. Anbar

## Geological background of the Kamura section

The Kamura section (32.7552 °N, 131.3386 °E) is located close to Shioinouso village, 5.6 km northeast of Takachiho-cho in Miyazaki Prefecture, in the center of Kyushu Island, Japan ([Isozaki et al., 2007](#); [Zhang et al., 2017](#)). The Kamura section is located within the Chichibu Belt, which is a Jurassic accretionary complex belt in southwestern Japan and comprises a structurally complicated aggregate of metamorphosed Upper Paleozoic and Mesozoic sedimentary rocks ([Isozaki, 2009](#); [Musashi et al., 2001](#); [Sano and Nakashima, 1997](#)). Although now located in central Japan, the sedimentary succession at Kamura originally accumulated in the middle of the Panthalassic Ocean at peri-equatorial latitudes, as indicated by a paleomagnetic study ([Ando et al., 2001](#)).

The study section is lithologically divided into two units ([Sano and Nakashima, 1997](#); [Zhang et al., 2017](#)): the Mitai Formation and the Kamura Formation. The Mitai Formation is Late Permian in age, and is primarily composed of white to light gray limestone and dolomitic limestone. The Mitai Formation records a shallowing-upward succession from subtidal to intertidal facies ([Sano and Nakashima, 1997](#)). The Kamura Formation is latest Permian to Late Triassic in age, and is mainly composed of micritic, microbial, and bioclastic limestones. The lack of terrigenous clastics, such as coarse quartzo-feldspathic grains, in the two formations suggests that their origin was in a mid-oceanic setting far from continental areas ([Isozaki et al., 2007](#); [Musashi et al., 2001](#)).

Previous biostratigraphic studies using fusulinids, corals, bivalves, ammonoids, and conodonts ([Kambe, 1963](#); [Kanmera and Nakazawa, 1973](#); [Koike, 1979](#); [Watanabe et al., 1979](#); [Kanmera and Nishi, 1983](#); [Ota and Isozaki, 2000](#)) indicate that the Kamura section spans the mid-Permian to Late Triassic. Koike ([1996](#)) first confirmed that the Kamura section contains the Griesbachian (the earliest Triassic) interval by recognizing the conodonts *Hindeodus parvus* and *Isarcicella isarcica* in the lowermost Kamura Formation. The conodont biostratigraphy at Kamura has recently been updated by Zhang et al. ([2017](#)). The fusulinid taxa at Kamura are mostly of Tethyan affinity, and the ubiquitous occurrence of calcareous algae in the Mitai Formation suggests a shallow, warm tropical depositional environment ([Isozaki et al., 2007](#)).

The end-Permian mass extinction (EPME) horizon at Kamura has been placed at the Mitai-Kamura formation boundary by Koike ([1996](#)) and Zhang et al. ([2017](#)), which is at ~-0.15 m in our section. The Permian-Triassic boundary (PTB) at Kamura has been placed in the lowermost Kamura Formation based on the first appearance of the conodont *Hindeodus parvus* (Koike, [1996](#); [Zhang et al., 2017](#)), which is at 0.20 m in our section. The biostratigraphically

well-constrained EPME and PTB horizons as well as the high-resolution carbon isotope chemostratigraphic profile for the Kamura section ([Horacek et al., 2009](#); [Isozaki et al., 2007](#); [Zhang et al., 2017](#)) make it possible to precisely correlate it to other well-studied PTB sections globally. The samples used in this study are from the same sample suite that was analyzed for carbon and oxygen isotopes as well as for conodonts by Zhang et al. ([2017](#)).

### Analytical methods for U isotopes

Fresh carbonate samples collected in the field were crushed to small pieces in the lab. The fragments were cleaned using deionized water (DI water) and dried, and fresh fragments without veins were carefully chosen and powdered to ~200 mesh using a ball mill and silicon nitride jars.

The protocols for powder dissolution are summarized in Table S-1. In the first six steps, ~1.0–1.5 g of each sample was dissolved in 1 M hydrochloric acid (HCl) at room temperature. This protocol employed a 1.5× excess of HCl in order to ensure complete dissolution of the carbonate, thus avoiding U isotope fractionation from selective leaching of various carbonate phases. The solution was allowed to sit at room temperature for 24 h before centrifuging to separate the supernatant and undissolved residue. We compared carbonate dissolution protocols using 1M HCl, 1M Acetic Acid, and 3M HNO<sub>3</sub>, and found that all these methods yield indistinguishable  $\delta^{238}\text{U}$  provided that excess acid is available to ensure complete carbonate dissolution (Table S-2).

Digests were centrifuged and the supernatant was separated. Major, minor, and trace element concentrations were measured on a Thermo iCAP™ quadrupole inductively coupled plasma mass spectrometer (Q-ICP-MS) at the W. M. Keck Laboratory for Environmental Biogeochemistry at Arizona State University (ASU) on splits from each supernatant. Typical precision was better than 5% based on repeated analysis of in-run check standards.

Prior to column chemistry, appropriate amounts of the  $^{236}\text{U}$ : $^{233}\text{U}$  double spike were added to each sample based on measured uranium concentrations. The spike-sample mixtures were evaporated to dryness and re-dissolved in 3 N HNO<sub>3</sub>. Uranium was purified for isotopic analysis using the UTEVA method ([Brennecke et al., 2011](#); [Romaniello et al., 2013](#); [Weyer et al., 2008](#)). Purified U was dissolved in 0.32 M HNO<sub>3</sub> and diluted to a U concentration of 50 ppb. Uranium isotopes were measured at ASU on a Thermo-Finnigan Neptune multi-collector ICP-MS at low mass resolution. When using a 75  $\mu\text{l}/\text{min}$  nebulizer, a 50 ppb sample solution yielded 24–32 V of  $^{238}\text{U}$  signal on a  $10^{11} \Omega$  amplifier. The unprocessed standard solution CRM145 (50 ppb U) was analyzed after every two samples. A secondary standard CRM129a and an in-house Ricca ICP solution were measured after every fifteen analyses. Sample  $\delta^{238}\text{U}$  values were normalized by the average of the bracketing standards.

The U isotopic composition of standards CRM145, CRM129a, and Ricca was  $-0.00 \pm 0.07 \text{ ‰}$  ( $2\sigma$ ),  $-1.68 \pm 0.07 \text{ ‰}$  ( $2\sigma$ ), and  $-0.23 \pm 0.06 \text{ ‰}$  ( $2\sigma$ ), respectively. The results (including samples, summary of standards, and blanks) are given in the Supplementary Databases DR1-DR2.

Table DR1. Sample dissolution procedure

Dissolution step	Solvent	Time gap between steps
S1–S6	5mL 1M hydrochloric acid	10 minutes
S7	1mL 10M hydrochloric acid	
S9–S11	5mL 1M hydrochloric acid	10 minutes
Final volume	46 mL	

S denotes step, for instance, S1–S6 denotes steps 1 to 6.

Table DR2 A summary of results from different carbonate dissolution protocols

Sample	digestion methods	$\delta^{238}\text{U}$ (‰)
DW330-345-1	1M acetic acid	-0.49 ± 0.03
DW330-345-2	1M hydrochloric acid	-0.50 ± 0.04
DW330-345-3	ash at 750°C then dissolve in 3M nitric acid	-0.48 ± 0.02
DW435+450-1	1M acetic acid	-0.73 ± 0.03
DW435+450-2	1M hydrochloric acid	-0.75 ± 0.05
DW435+450-3	ash at 750°C then dissolve in 3M nitric acid	-0.75 ± 0.06
DXK-11 base-1	1M acetic acid	-0.81 ± 0.08
DXK-11 base-2	1M hydrochloric acid	-0.84 ± 0.03
DXK-11 base-3	ash at 750°C then dissolve in 3M nitric acid	-0.74 ± 0.06
DXK-2-1	1M acetic acid	0.33 ± 0.05
DXK-2-2	1M hydrochloric acid	0.37 ± 0.02
DXK-2-3	ash at 750°C then dissolve in 3M nitric acid	0.35 ± 0.07
DXK-32-1	1M acetic acid	-0.28 ± 0.07
DXK-32-2	1M hydrochloric acid	-0.27 ± 0.04
DXK-32-3	ash at 750°C then dissolve in 3M nitric acid	--

Note: -- denotes data not available. DW330-345, DW435+450, DXK-11, DXK-2, and DXK-32 are samples numbers, these samples are of Permian-Triassic age.

### Evaluation of carbonate diagenesis, detrital contamination and dolomitization

Marine carbonate sediments can faithfully record chemical signatures of seawater provided that post-depositional processes have not caused significant alteration. To assess diagenesis, we used standard geochemical criteria based on trace element ratios to evaluate the influence of meteoric or burial fluids on measured U isotope signatures. The concentrations of trace elements (Sr, Mn, and Fe) that substitute into the lattice of carbonate minerals is governed by their distribution coefficients and their concentrations in the fluids from which carbonates precipitate. Modern, well-oxygenated seawater is high in Sr relative to Mn and Fe such that primary precipitates and early diagenetic phases formed in the presence of seawater are generally enriched in Sr relative to Mn and Fe ([Banner and Hanson, 1990](#)). This is particularly true for aragonite because of the high distribution coefficient for Sr into aragonite compared to other carbonate minerals ([Veizer, 1983](#)). Early fabric-retentive dolostone can also be enriched in Sr relative to Mn and Fe, although dolomite generally has a lower preference for Sr ([Vahrenkamp and Swart, 1990](#)) and a higher preference for Mn and Fe ([Mazzullo, 1992](#)) compared to calcite.

In contrast, meteoric and burial fluids tend to be depleted in Sr relative to seawater ([Banner and Hanson, 1990](#)). The recrystallization process also acts to expel Sr from the lattice of carbonate minerals because of its relatively large ionic radius compared to Ca in calcite and dolomite, which are the most important secondary phases ([Rimstidt et al., 1998](#)). As a result,

meteoric or burial diagenetic phases are often depleted in Sr relative to precursor marine phases. Burial fluids can also be substantially enriched in Mn and Fe, particularly under reducing conditions (Veizer, 1983), leading to Mn and Fe enrichment in burial diagenetic phases. Meteoric fluids are variable in their Mn and Fe content—depending largely on redox conditions—such that meteoric calcite phases can be characterized by enrichment or depletion of Mn and Fe.

These general relationships have led to the establishment of widely used proxies such as the Mn/Sr ratio to assess the fidelity of primary geochemical signatures in carbonate rocks. For example, Kaufman and Knoll (Kaufman and Knoll, 1995) suggested that both limestone and dolostone with Mn/Sr ratios < 10 can be expected to retain their primary carbon isotopic signatures. In this study, we used a more conservative Mn/Sr ratio of 1 for identifying unaltered primary marine carbonates (also used by Lau et al., (2016)). In the Kamura section, all samples have Sr concentrations of >150 ppm with 9 out of 17 samples having Sr concentrations of >500 ppm (Fig. S1). Most samples have low Mn contents (<102 ppm for 12 out of 17 samples) and low Mn/Sr ratios (15 out of 17 samples have Mn/Sr ratios of <0.6, and the remaining two samples have ratios of 2.1 and 6.8; Fig. S1). These results indicate that the Kamura samples are generally well preserved and likely to retain primary marine geochemical signatures.

The Ce anomalies in our samples range between 0.27 and 0.54 with exception of only one sample gives a Ce anomaly of 0.74 (Fig. S1H, Ce anomalies are calculated according to Ling et al. (2013)). These values suggest the local depositional condition at Kamura was persistently oxic (Ling et al., 2013). The lack statistically significant correlations between  $\delta^{238}\text{U}$  and Ce anomalies (Table S-3) further indicate that the  $\delta^{238}\text{U}$  trend at Kamura is not related to local redox variations.

When evaluating detrital contamination, we used detrital indicators such as Rb/Sr ratios and Al concentrations (cf. (Ling et al., 2013)). Among samples with Mn/Sr < 1, only those samples with Rb/Sr < 0.02 and Al (wt.%) < 0.35% (all samples met this criterion) were used in our analysis of secular redox patterns. Finally, for samples meeting the Mn/Sr < 1, Rb/Sr < 0.02 and Al < 0.35% thresholds, we examined their U/Al ratios to determine the degree of authigenic U enrichment. Relative to the U/Al ratio of average upper continental crust (~0.331 ppm/wt.%; (Rudnick and Gao, 2003)), all samples are enriched in U by approximately two orders of magnitude (Fig. S1). This demonstrates that the majority of U in our samples is authigenic rather than detrital in origin.

Romaniello et al. (2013) observed U-isotope changes associated with dolomitization in a modern Bahamian tidal pond, as reflected in a strong correlation of  $\delta^{238}\text{U}$  with Mg/Ca ( $R^2 = 0.96$ ), suggesting possible U-isotope fractionation linked to dolomitization. The reason for this strong correlation remain unclear. This seems to be a special, spatially restricted case, however. In the Kamura samples,  $\delta^{238}\text{U}$  and Mg/Ca show only a moderate correlation ( $R^2 = 0.41$ ), and positive sign of this relationship is opposite that of the Bahamian carbonates. This indicates that the dolomitization process probably does not have a systematic effect on carbonate U-isotope compositions, although this issue requires further investigation.

A recent texture-specific  $\delta^{238}\text{U}$  study reported high variability in  $\delta^{238}\text{U}$  values between different carbonate components (Hood et al., 2016). To better understand the range and variability of  $\delta^{238}\text{U}$  in bulk carbonate sediments, we have conducted a 16-step leaching experiment using acetic acid with different molarities to sequentially extract different carbonate components in carbonate sediments (Table S-5 and Fig. S2; see discussions below). In agreement with Hood et al. (2016), our leaching results show large variability in  $\delta^{238}\text{U}$  values (up to 0.5 ‰)

among different leaching steps, indicating that  $\delta^{238}\text{U}$  are highly inhomogeneous between different carbonate components. However, contrary to [Hood et al. \(2016\)](#) who argue that U isotopes in bulk carbonates are seriously reset by diagenesis, our study strongly suggests that the bulk U isotopes are not typically isotopically reset and that U isotopes in bulk carbonates are reliable recorders. Even though  $\delta^{238}\text{U}$  values vary between different carbonate components, the weighted sums of  $\delta^{238}\text{U}$  of all leaching steps are indistinguishable to  $\delta^{238}\text{U}$  of the bulk analysis (Table S-5). The possible reason for this is that typically U isotopes are locally redistributed and fractionated during recrystallization and this results in different isotopic compositions between different generations of carbonate phases. However, since this process may happen in a closed system, the bulk U isotopic composition of the carbonates remains the same.

### Detailed comparison of Permian-Triassic $\delta^{238}\text{U}$ records at Panthalassic and Tethyan sites

Here, we compare our new  $\delta^{238}\text{U}$  record from Kamura (Japan) with published  $\delta^{238}\text{U}$  records for three other PTB sections: the Dawen (China) section studied by [Brenneka et al. \(2011\)](#), and the Dajiang (China) and Taşkent (Turkey) sections studied by [Lau et al. \(2016\)](#) (Fig. 2 of main text). These sections were widely distributed paleogeographically, as shown in Figure S3. All four sections have been correlated in detail to the well-dated Meishan section using a combination of conodont biostratigraphy and  $\delta^{13}\text{C}$  chemostratigraphy. According to [Burgess et al. \(2014\)](#), the ages of the EPME and PTB horizons are  $251.941 \pm 0.037$  Ma and  $251.902 \pm 0.024$  Ma, respectively. The EPME is recognized as the transition from the *Clarkina yini* Zone to the *Clarkina meishanensis* Zone, and the PTB is defined by the first appearance datum of *Hindeodus parvus*. According to [Burgess et al. \(2014\)](#), an extrapolated age of 251.323 Ma has been assigned to the first positive shift of the  $\delta^{13}\text{C}$  in the Lower Triassic  $\delta^{13}\text{C}$  records. With these ages, sedimentation rates can be calculated for two intervals at each section: (1) between the EPME and PTB, and (2) between the PTB and the first positive shift in  $\delta^{13}\text{C}$ . Based on these sedimentation rate data, we calculated the age for each individual sample in each section. Using this method, the  $\delta^{13}\text{C}$  excursions in all four sections are well-aligned (Fig. 2A in main text).

We are aware that there is another  $\delta^{238}\text{U}$  study from a South China section by [Elrick et al. \(2017\)](#), who also documented an abrupt negative  $\delta^{238}\text{U}$  shift of 0.4–0.5 ‰ across the EPME. However, their primary focus was on the Middle to Upper Permian, and they analyzed only a few samples through the PTB interval. Thus, this study has been excluded from the present compilation which focuses on high-resolution records across the EPME.

The compiled  $\delta^{238}\text{U}$  records show 0.2–0.4 ‰ (with a mean of 0.3 ‰) scatter around the EPME (Fig. 2B), the source of which is not fully understood yet. It may reflect differential incorporation of  $^{238}\text{U}$ -enriched U(IV) from anoxic porewaters during early diagenesis, similar to the Bahamian carbonate sediments ([Romaniello et al., 2013](#)) or variation in pore water aqueous U-speciation during syndepositional carbonate recrystallization ([Chen et al., 2016](#)). Porewater data from deep drill cores in the Bahamas suggest that the potential for alteration following burial may be limited because the pore waters are anoxic rendering U essentially immobile ([Henderson et al., 1999](#)). Our interpretation is that following syndepositional diagenesis which imparts a  $+0.3 \pm 0.1$  ‰ offset in  $\delta^{238}\text{U}$ , later burial diagenesis has no measurable effect on the bulk sediment U-isotope compositions because the sediments are essentially closed to U exchange. On this basis, we have applied a  $+0.3 \pm 0.1$  ‰ correction to measured PTB bulk carbonate  $\delta^{238}\text{U}$  values prior to mass balance calculations (presented below).

The available compilation of PTB  $\delta^{238}\text{U}$  records strongly supports the inference that all observed  $\delta^{238}\text{U}$  variations are primary and represent secular changes in Permian-Triassic seawater  $\delta^{238}\text{U}$ . This inference is based on the observation that multiple PTB sections have recorded the same  $\delta^{238}\text{U}$  signal despite their manifest differences. First, these sections are located in different ocean basins and thus unlikely to have similar diagenetic histories. Second, as discussed above, the Mn and Sr concentrations,  $\delta^{18}\text{O}$  values, and Mn/Sr ratios are commonly used to evaluate the extent of carbonate diagenesis. Although this study and all prior studies have applied conservative cutoffs of these diagenetic proxies to screen for potential alterations, the combined sections exhibit different Mn and Sr concentrations,  $\delta^{18}\text{O}$  values, and Mn/Sr ratios, as well as different patterns of correlation of  $\delta^{238}\text{U}$  with these proxies, thus indicating that these sections experienced different diagenetic histories (Table S-3, Fig. S5 and Fig. S6). Third, the U/Al ratios in carbonates are typically used to evaluate levels of authigenic U enrichment, these sections yield different U concentrations and U/Al ratios, indicating that levels of authigenic U factors vary between the sections (Table S-3, Fig. S5 and Fig. S6). Fourth, the Mg/Ca molar ratios can be used to indicate the extent of dolomitization, these sections have different Mg/Ca molar ratios and different patterns of  $\delta^{238}\text{U}$ -Mg/Ca covariation, indicating variations in degree of dolomitization between the sections (Table S-3, Fig. S5 and Fig. S6). Despite all these differences, after screening for potential diagenetic influences using well-established carbonate diagenetic indicators (e.g., Mn and Sr contents, Mn/Sr ratios, and  $\delta^{18}\text{O}$ ), all of the studied PTB sections record the same  $\delta^{238}\text{U}$  trend through the PTB interval.

Table DR3. Cross-correlation coefficients ( $R^2$ ) and p-values calculated to test the influence of diagenetic indicators on  $\delta^{238}\text{U}$ . “--” denotes related data are not available in the original publication.

Kamura section, Japan	$R^2$	$p$ -value
$\delta^{238}\text{U}$ vs. $\delta^{13}\text{C}$	0.50	<0.01
$\delta^{238}\text{U}$ vs. Mg/Ca (mol:mol)	0.38	<0.01
$\delta^{238}\text{U}$ vs. $\delta^{18}\text{O}$	0.02	0.60
$\delta^{238}\text{U}$ vs. Sr concentration	0.70	<0.01
$\delta^{238}\text{U}$ vs. Mn concentration	0.16	0.12
$\delta^{238}\text{U}$ vs. Mn/Sr	0.27	0.03
$\delta^{238}\text{U}$ vs. U/Al (ppm/w.t.%)	0.60	<0.01
$\delta^{238}\text{U}$ vs. Ce anomalies	0.27	0.29
Dawen section, South China	$R^2$	$p$ -value
$\delta^{238}\text{U}$ vs. $\delta^{13}\text{C}$	0.18	<0.01
$\delta^{238}\text{U}$ vs. Mg/Ca (mol:mol)	--	--
$\delta^{238}\text{U}$ vs. $\delta^{18}\text{O}$	--	--
$\delta^{238}\text{U}$ vs. Mn/Sr	--	--
$\delta^{238}\text{U}$ vs. U/Al (ppm/w.t.%)	0.24	<0.01
Dajiang, China	$R^2$	$p$ -value
$\delta^{238}\text{U}$ vs. $\delta^{13}\text{C}$	0.38	0.02
$\delta^{238}\text{U}$ vs. Mg/Ca (mol:mol)	0.00	0.93
$\delta^{238}\text{U}$ vs. $\delta^{18}\text{O}$	0.00	0.94
$\delta^{238}\text{U}$ vs. Mn/Sr	0.01	0.78
$\delta^{238}\text{U}$ vs. U/Al (ppm/w.t.%)	0.37	0.03

Taşkent, Turkey	$R^2$	$p$ -value
$\delta^{238}\text{U}$ vs. $\delta^{13}\text{C}$	0.62	<0.01
$\delta^{238}\text{U}$ vs. Mg/Ca (mol:mol)	0.00	0.96
$\delta^{238}\text{U}$ vs. $\delta^{18}\text{O}$	0.28	0.03
$\delta^{238}\text{U}$ vs. Mn/Sr	0.015	0.14
$\delta^{238}\text{U}$ vs. U/Al (ppm/w.t.%)	0.19	0.09

Note: when  $p(\alpha) < 0.05$ , then  $\delta^{238}\text{U}$  shows a statistically significant correlation with the proxy; if  $p(\alpha) > 0.05$ , then  $\delta^{238}\text{U}$  does not show a statistically correlation with the proxy.

## The lumped oxic sinks and other sinks and their associated fractionation factors

A simplified schematic of the major sources and sinks of U in the modern ocean along with the isotopic compositions of sources and isotopic fractionations associated with sinks is presented in Figure S7. Following Wang et al. (2016), in order to simplify the mass balance calculations presented below, several types of sinks are lumped into a single oxic sink, including Fe-Mn crusts, pelagic clays, low-temperature and high-temperature oceanic crustal alteration, marine carbonates, and coastal retention. Additionally, the oxic sink and suboxic sink are lumped into a single sink (“other”) in order to simplify calculations of anoxic/euxinic sink fluxes. The overall U isotope fractionation factors for lumped sinks are calculated as the weighted average of fractionations associated with their constituent sinks. The fractionation factors between the lumped oxic sink and seawater and between the lumped other sink and seawater are 0.005‰ ( $\Delta_{\text{oxic}}$ ) and 0.043‰ ( $\Delta_{\text{other}}$ ).

## Uranium isotope mass balance constraints on U removal to anoxic/euxinic sinks

Changes in U removal to anoxic sediments, as summarized in the main text, can be quantified using a mass balance relationship based on the fractions of the anoxic/euxinic sinks and their isotopic compositions (following Montoya-Pino et al., 2010):

$$\delta^{238}\text{U}_{\text{input}} = (f_{\text{anoxic}} \times \delta^{238}\text{U}_{\text{anoxic}}) + (f_{\text{other}} \times \delta^{238}\text{U}_{\text{other}}) \quad (1)$$

$$\delta^{238}\text{U}_{\text{anoxic}} = \delta^{238}\text{U}_{\text{seawater}} + \Delta_{\text{anoxic}} \quad (2)$$

$$\delta^{238}\text{U}_{\text{other}} = \delta^{238}\text{U}_{\text{seawater}} + \Delta_{\text{other}} \quad (3)$$

$$f_{\text{anoxic}} + f_{\text{other}} = 1 \quad (4)$$

The subscripts *input*, *anoxic*, and *other* denote the riverine input, anoxic/euxinic sink, and other sedimentary sinks, respectively, and  $f_{\text{anoxic}}$  represents the fraction of the riverine U input that is deposited in anoxic/euxinic sediments. Following Montoya-Pino et al. (2010) and Brennecka et al. (2011), we assume: (1) isotopically constant U input from rivers ( $\delta^{238}\text{U}_{\text{river}}$ ) over geologic time with an average value of  $-0.34$  ‰ (Andersen et al., 2016; Noordmann et al., 2016); (2) a constant isotopic fractionation between seawater and the other sinks ( $\Delta_{\text{other}}$ ) of  $+0.043$  ‰ (Fig. S7); and (3) a constant isotopic fractionation between seawater and anoxic/euxinic sinks ( $\Delta_{\text{anoxic}}$ ) of  $+0.6$  ‰. This last value is an average from modern anoxic environments and similar to  $\Delta_{\text{anoxic}}$  values that have been used in previous U isotope modeling investigations (Brennecka et al.,

2011; Dahl et al., 2014; Dahl et al., 2017; Elrick et al., 2017; Lau et al., 2016). Solving equations 1–4, we have:

$$f_{\text{anoxic}} = (\delta^{238}\text{U}_{\text{river}} - \delta^{238}\text{U}_{\text{seawater}} - \Delta_{\text{other}}) / (\Delta_{\text{anoxic}} - \Delta_{\text{other}}) \quad (5)$$

Using the parameters above, we can solve for  $f_{\text{anoxic}}$  for each sample analyzed. The results are shown in Figure 2D of the main text. Prior to making these calculations, we adjusted measured  $\delta^{238}\text{U}$  values by 0.1 ‰ to 0.3 ‰ to account for diagenetic offsets relative to contemporaneous seawater  $\delta^{238}\text{U}$ , as discussed above:

$$\delta^{238}\text{U}_{\text{seawater}} = \delta^{238}\text{U}_{\text{carbonate}} - \Delta_{\text{diagenetic offset}} \quad (6)$$

### Estimating the timing of onset of oceanic anoxia

We evaluated the timing of onset of oceanic anoxia based on the observed initial negative shift in  $\delta^{238}\text{U}$  relative to stable Late Permian background values. To more accurately identify the timing of the initial negative shift, we applied a robust LOWESS (Locally Weighted Scatterplot Smoothing) smoothing function to smooth the compiled data in Figure 2B of the main text. A tapered integration window of 0.2 Myr was used in the smoothing function. The smoothed  $\delta^{238}\text{U}$  curve is shown in Figure S8. The initial negative shift in  $\delta^{238}\text{U}$  occurred <70 kyr before the EPME, representing the lag between the onset of oceanic anoxia and the mass extinction event. Although this estimate is associated with some age-model uncertainties related to compiling data from multiple sections, this analysis serves to show that the expansion of oceanic anoxia probably predated the mass extinction event, although only by a limited interval (<70 kyr).

### Sequential extraction experiments

To better understand the range and variability of  $\delta^{238}\text{U}$  in bulk carbonate sediments, we conducted a leaching experiment using acetic acid with different molarities to sequentially extract carbonate components in Permian-Triassic sediments. In this experiment, we analyzed five samples, two from the Permian-Triassic Kamura section (KAMD-20 and KAMD-31) and three from the modern Bahamian carbonate platform (including one modern coral sample and two sediment core samples: core 1 40-42 cm, and core 4 24-28 cm, which were previously studied by Romaniello et al. (2013)). We used a 16-step sequential extraction protocol following the methods of Liu et al. (2013), as summarized in Table S-4.

Table DR4. Extraction protocol

Leaching step	Label	Leaching agent	pH
S1-S2	1	30 mL 1 N ammonium acetate and a few drops of H <sub>2</sub> O <sub>2</sub>	7.5
S3-S9	2	30 mL 0.25% (v/v) acetic acid for each step	
S10-S12	3	30 mL 1% (v/v) acetic acid for each step	
S13-S14	4	30 mL 5% (v/v) acetic acid for each step	
S15-S16	5	50 mL 10% (v/v) acetic acid for each step	

Note that after each step the sample was rinsed and ultrasonicated in DI water for 10 minutes, and then centrifuged at 4000 rpm for 5 min to separate the supernatant and undissolved residue. Major, minor, and trace element concentrations were measured on a Thermo iCAP™ quadrupole inductively coupled plasma mass spectrometer (Q-ICP-MS) at the W. M. Keck Laboratory for Environmental Biogeochemistry at Arizona State University (ASU) on splits from each supernatant.

Owing to low U concentrations for some samples, we combined Steps S1 and S2 (= Label 1), Steps S3 to S9 (= Label 2), Steps S10 to S12 (= Label 3), Steps S13 and S14 (= Label 4), and Steps S14 to S16 (= Label 5) for the purpose of U isotope analysis. U isotope analytical methods were identical to those of the main study (see methods description above), and the results are given in Table S-5.

One of the key questions that we investigated is whether the measured isotopic variations in each sample were actually generated as an artefact of isotopic fractionation during the sequential leaching experiments. The modern coral sample showed no isotopic fractionation during the sequential leaching experiments, since the results for Labels 1 to 5 are statistically indistinguishable (Fig. S2, Table S-5). We therefore tentatively suggest that differences in  $\delta^{238}\text{U}$  among leaching steps for the other samples reflect true isotopic inhomogeneities within these samples (Fig. S2).

For the two Permian-Triassic samples and two modern Bahamian carbonate sediments, the leaching experiments yielded large differences in  $\delta^{238}\text{U}$  (to  $\sim 0.5$  ‰) among different fractions. We infer that different carbonate components of these samples have different  $\delta^{238}\text{U}$  compositions, and that partial carbonate leaching leads to expression of these isotopic differences. Our leaching results thus agree with Hood et al. (2016) that  $\delta^{238}\text{U}$  varies among different carbonate fractions. However, the weighted sums of  $\delta^{238}\text{U}$  of all leaching steps are indistinguishable to those of the bulk analysis (Table S-5), indicating that the bulk U isotopes are not typically isotopically reset.

Table DR5. A summary of leaching results

Label	Leaching agents	Sample number	$\delta^{238}\text{U}$ (‰)	Amount of U (ng)	percent of U (%)
bulk analysis	1 M hydrochloric acid	Modern coral	-0.40	2553.00	
1	ammonium acetate	Coral-1	-0.39	16.52	1
2	0.25% acetic acid	Coral-2	-0.43	322.45	13
3	1% acetic acid	Coral-3	-0.41	1293.06	51
4	5% acetic acid	Coral-4	-0.41	766.91	30
5	10% acetic acid	Coral-5	-0.40	161.53	6
<b>weighted sums</b>			<b>-0.41</b>		
bulk analysis	1 M hydrochloric acid	Core 1 40-42cm	0.14	5435.66	
1	ammonium acetate	C1-1	0.40	655.22	13
2	0.25% acetic acid	C1-2	0.34	1416.65	29
3	1% acetic acid	C1-3	0.07	1343.63	27
4	5% acetic acid	C1-4	-0.09	1305.14	27
5	10% acetic acid	C1-5	0.06	186.55	4
<b>weighted sums</b>			<b>0.15</b>		
bulk analysis	1 M hydrochloric acid	Core 4 24-28cm	-0.51	--	
1	ammonium acetate	C4-1	-0.79	20.28	1
2	0.25% acetic acid	C4-2	-0.80	211.80	6
3	1% acetic acid	C4-3	-0.65	970.19	27
4	5% acetic acid	C4-4	-0.54	1925.58	53
5	10% acetic acid	C4-5	-0.62	494.52	14
<b>weighted sums</b>			<b>-0.59</b>		
bulk analysis	1 M hydrochloric acid	PT carbonates	0.03	184.86	
1	ammonium acetate	KAMD-20-1	-0.06	12.11	11

2	0.25% acetic acid	KAMD-20-2	0.02	27.75	25
3	1% acetic acid	KAMD-20-3	0.03	29.74	27
4	5% acetic acid	KAMD-20-4	0.14	31.46	28
5	10% acetic acid	KAMD-20-5	0.17	10.07	9
<b>weighted sums</b>			<b>0.06</b>		
bulk analysis	1 M hydrochloric acid	PT carbonates	-0.12	1021.59	
1	ammonium acetate	KAMD-31-1	-0.20	100.14	6
2	0.25% acetic acid	KAMD-31-2	-0.04	248.46	15
3	1% acetic acid	KAMD-31-3	-0.04	782.70	46
4	5% acetic acid	KAMD-31-4	-0.07	422.00	25
5	10% acetic acid	KAMD-31-5	-0.46	154.32	9
<b>weighted sums</b>			<b>-0.10</b>		

Note that the weighted sums come from the weighted sum of all the leaching steps (step 1 to step 5). The weighted sums are indistinguishable to the bulk analysis. Modern coral, Core 1 40-42cm, and Core 4 24-28cm are three recent carbonate precipitates from the modern Bahamian carbonate platform, see Romaniello et al. (2013) for sample details. KAMD-20 and KAMD-31 are two Permian-Triassic (PT) carbonates from the Kamura section in Japan.

## References

- Andersen, M. B., Vance, D., Morford, J. L., Bura-Nakić, E., Breitenbach, S. F. M., and Och, L., 2016, Closing in on the marine  $^{238}\text{U}/^{235}\text{U}$  budget: *Chemical Geology*, v. 420, p. 11-22, doi: 10.1016/j.chemgeo.2015.10.041.
- Ando, A., Kodama, K., and Kojima, S., 2001, Low-latitude and Southern Hemisphere origin of Anisian (Triassic) bedded chert in the Inuyama area, Mino terrane, central Japan: *Journal of Geophysical Research: Solid Earth*, v. 106, no. B2, p. 1973-1986, doi: 10.1029/2000JB900305.
- Banner, J. L., and Hanson, G. N., 1990, Calculation of simultaneous isotopic and trace element variations during water-rock interaction with applications to carbonate diagenesis: *Geochimica et Cosmochimica Acta*, v. 54, no. 11, p. 3123-3137, doi: 10.1016/0016-7037(90)90128-8.
- Brennecka, G. A., Herrmann, A. D., Algeo, T. J., and Anbar, A. D., 2011, Rapid expansion of oceanic anoxia immediately before the end-Permian mass extinction: *Proceedings of the National Academy of Sciences (U.S.A.)*, v. 108, no. 43, p. 17631-17634, doi: 10.1073/pnas.1106039108.
- Burgess, S. D., Bowring, S., and Shen, S. Z., 2014, High-precision timeline for Earth's most severe extinction: *Proceedings of the National Academy of Sciences (U.S.A.)*, v. 111, no. 9, p. 3316-3321, doi: 10.1073/pnas.1317692111.
- Chen, J., Beatty, T. W., Henderson, C. M., and Rowe, H., 2009, Conodont biostratigraphy across the Permian–Triassic boundary at the Dawen section, Great Bank of Guizhou, Guizhou Province, South China: Implications for the Late Permian extinction and correlation with Meishan: *Journal of Asian Earth Sciences*, v. 36, no. 6, p. 442-458, doi.org/10.1016/j.jseaes.2008.08.002.
- Chen, X., Romaniello, S. J., Herrmann, A. D., Wasylenki, L. E., and Anbar, A. D., 2016, Uranium isotope fractionation during coprecipitation with aragonite and calcite: *Geochimica et Cosmochimica Acta*, v. 188, p. 189-207, doi: 10.1016/j.gca.2016.05.022.
- Dahl, T. W., Boyle, R. A., Canfield, D. E., Connelly, J. N., Gill, B. C., Lenton, T. M., and Bizzarro, M., 2014, Uranium isotopes distinguish two geochemically distinct stages during the later Cambrian SPICE event: *Earth and Planetary Science Letters*, v. 401, p. 313-326, doi: 10.1016/j.epsl.2014.05.043.
- Dahl, T. W., Connelly, J. N., Kouchinsky, A., Gill, B. C., Månsson, S. F., and Bizzarro, M., 2017, Reorganisation of Earth's biogeochemical cycles briefly oxygenated the oceans 520 Myr ago: *Geochemical Perspectives Letters*, p. 210-220, doi: 10.7185/geochemlet.1724.
- Elrick, M., Polyak, V., Algeo, T. J., Romaniello, S., Asmerom, Y., Herrmann, A. D., Anbar, A. D., Zhao, L., and Chen, Z.-Q., 2016, Global-ocean redox variation during the middle-late Permian through Early Triassic based on uranium isotope and Th/U trends of marine carbonates: *Geology*, v. 45, no. 2, p. 163-166, doi: <https://doi.org/10.1130/G38585.1>.
- Henderson, G. M., Slowey, N. C., and Haddad, G. A., 1999, Fluid flow through carbonate platforms: constraints from  $^{234}\text{U}/^{238}\text{U}$  and  $\text{Cl}^-$  in Bahamas pore-waters: *Earth and Planetary Science Letters*, v. 169, no. 1-2, p. 99-111, doi: 10.1016/S0012-821X(99)00065-5.
- Hood, A. v. S., Planavsky, N. J., Wallace, M. W., Wang, X., Bellefroid, E. J., Gueguen, B., and Cole, D. B., 2016, Integrated geochemical-petrographic insights from component-

- selective  $\delta^{238}\text{U}$  of Cryogenian marine carbonates: *Geology*, v. 44, no. 11, p. 935-938, doi: <https://doi.org/10.1130/G38533.1>.
- Horacek, M., Koike, T., and Richoz, S., 2009, Lower Triassic  $\delta^{13}\text{C}$  isotope curve from shallow-marine carbonates in Japan, Panthalassa realm: Confirmation of the Tethys  $\delta^{13}\text{C}$  curve: *Journal of Asian Earth Sciences*, v. 36, no. 6, p. 481-490, doi.org/10.1016/j.jseaes.2008.05.005.
- Isozaki, Y., 2009, Integrated “plume winter” scenario for the double-phased extinction during the Paleozoic–Mesozoic transition: The G-LB and P-TB events from a Panthalassan perspective: *Journal of Asian Earth Sciences*, v. 36, no. 6, p. 459-480, doi:10.1016/j.jseaes.2009.05.006.
- Isozaki, Y., Kawahata, H., and Ota, A., 2007, A unique carbon isotope record across the Guadalupian–Lopingian (Middle–Upper Permian) boundary in mid-oceanic paleo-atoll carbonates: The high-productivity “Kamura event” and its collapse in Panthalassa: *Global and Planetary Change*, v. 55, no. 1-3, p. 21-38, doi.org/10.1016/j.gloplacha.2006.06.006.
- Kambe, N., 1963. On the boundary between the Permian and Triassic Systems in Japan with the description of the Permo-Triassic formations at Takachiho-cho, Miyazaki Prefecture in Kyushu and the Skytic fossils contained. In: *Geological Survey of Japan, Report 198*, (68 pp.).
- Kanmera, K., Nakazawa, K., 1973. Permian–Triassic relationships and faunal changes in the eastern Tethys. In: Logan, A., Hills, L.V. (Eds.), *The Permian and Triassic Systems and their Mutual Boundary*. Canadian Society of Petroleum Geologists Memoir 2pp. 100–119.
- Kanmera, K., Nishi, H., 1983. Accreted oceanic reef complex in Southwest Japan. In: Hashimoto, M., Uyeda, S. (Eds.), *Accretion Tectonics in the Circum-Pacific Regions*. Terra Science, Tokyo, Japan, pp. 195–206.
- Kaufman, A., and Knoll, A., 1995, Neoproterozoic variations in the C-isotopic composition of seawater: stratigraphic and biogeochemical implications: *Precambrian Research*, v. 73, no. 1-4, p. 27-49, doi: 10.1016/0301-9268(94)00070-8.
- Koike, T., 1979. Conodont biostratigraphy of Triassic Tahoe limestone in western Shikoku, SW Japan. In: Igo, H., Koike, T. (Eds.), *Biostratigraphy of Permian and Triassic Conodonts and Holothurian Sclerites in Japan*. Committee of Prof. M. Kanuma Retirement Ceremony, Tokyo, Japan, pp. 115–126.
- Koike, T., 1996, The first occurrence of Griesbachian conodonts in Japan: *Paleontological Society of Japan, N.S.*, v. 181, p. 337-346, doi.org/10.14825/prpsj1951.1996.181\_337.
- Lau, K. V., Maher, K., Altiner, D., Kelley, B. M., Kump, L. R., Lehrmann, D. J., Silva-Tamayo, J. C., Weaver, K. L., Yu, M., and Payne, J. L., 2016, Marine anoxia and delayed Earth system recovery after the end-Permian extinction: *Proceedings of the National Academy of Sciences*, v. 113, no. 9, p. 2360–2365, doi: 10.1073/pnas.1515080113.
- Ling, H.-F., Chen, X., Li, D., Wang, D., Shields-Zhou, G. A., and Zhu, M., 2013, Cerium anomaly variations in Ediacaran–earliest Cambrian carbonates from the Yangtze Gorges area, South China: Implications for oxygenation of coeval shallow seawater: *Precambrian Research*, v. 225, p. 110-127, doi: 10.1016/j.precamres.2011.10.011.
- Liu, C., Wang, Z., and Raub, T. D., 2013, Geochemical constraints on the origin of Marinoan cap dolostones from Nuccaleena Formation, South Australia: *Chemical Geology*, v. 351, p. 95-104, doi: 10.1016/j.chemgeo.2013.05.012.
- Mazzullo, S. J., 1992, Geochemical and neomorphic alteration of dolomite: a review: *Carbonates and Evaporites* 7.1, p. 21-37.

- Montoya-Pino, C., Weyer, S., Anbar, A. D., Pross, J., Oschmann, W., van de Schootbrugge, B., and Arz, H. W., 2010, Global enhancement of ocean anoxia during Oceanic Anoxic Event 2: A quantitative approach using U isotopes: *Geology*, v. 38, no. 4, p. 315-318, doi: <https://doi.org/10.1130/G30652.1>.
- Musashi, M., Isozaki, Y., Koike, T., and Kreulen, R., 2001, Stable carbon isotope signature in mid-Panthalassa shallow-water carbonates across the Permo–Triassic boundary: evidence for  $^{13}\text{C}$ -depleted superocean: *Earth and Planetary Science Letters*, v. 191, no. 1-2, p. 9-20, doi: 10.1016/S0012-821X(01)00398-3.
- Noordmann, J., Weyer, S., Georg, R. B., Jons, S., and Sharma, M., 2016,  $^{238}\text{U}/^{235}\text{U}$  isotope ratios of crustal material, rivers and products of hydrothermal alteration: new insights on the oceanic U isotope mass balance: *Isotopes in Environmental and Health Studies*, v. 52, no. 1-2, p. 141-163, doi: 10.1080/10256016.2015.1047449.
- Ota, A., Isozaki, Y., 2000. Stratigraphy of the Upper Permian Kamura Limestone in Southwest Japan: Ancient cap reef on a mid-oceanic paleo-seamount (abstract). *EOS Trans. Am. Geophys. Union* 81, 218.
- Payne, J. L., Lehrmann, D. J., Follett, D., Seibel, M., Kump, L. R., Riccardi, A., Altiner, D., Sano, H., and Wei, J., 2007, Erosional truncation of uppermost Permian shallow-marine carbonates and implications for Permian-Triassic boundary events: *Geological Society of America Bulletin*, v. 119, no. 7-8, p. 771-784, doi: 10.1130/B26588.1.
- Rimstidt, J. D., Balog, A., and Webb, J., 1998, Distribution of trace elements between carbonate minerals and aqueous solutions: *Geochimica et Cosmochimica Acta*, v. 62, no. 11, p. 1851-1863, doi:10.1016/S0016-7037(98)00125-2.
- Romaniello, S. J., Herrmann, A. D., and Anbar, A. D., 2013, Uranium concentrations and  $^{238}\text{U}/^{235}\text{U}$  isotope ratios in modern carbonates from the Bahamas: Assessing a novel paleoredox proxy: *Chemical Geology*, v. 362, p. 305-316, doi: 10.1016/j.chemgeo.2013.10.002.
- Rudnick, R. L., and Gao, S., 2003, Major elements of Earth Crust: *Treatise on Geochemistry*, v. 3, p. 1-64, doi: 10.1016/B978-0-08-095975-7.00301-6.
- Sano, H., and Nakashima, K., 1997, Lowermost Triassic (Griesbachian) microbial bindstone-cementstone facies, southwest Japan: *Facies*, v. 36, no. 1, p. 1–24.
- Tissot, F. L. H., and Dauphas, N., 2015, Uranium isotopic compositions of the crust and ocean: Age corrections, U budget and global extent of modern anoxia: *Geochimica et Cosmochimica Acta*, v. 167, p. 113-143, doi: 10.1016/j.gca.2015.06.034.
- Vahrenkamp, V. C., and Swart, P. K., 1990, New distribution coefficient for the incorporation of strontium into dolomite and its implications for the formation of ancient dolomites: *Geology*, v. 18, no. 5, p. 387, doi: [https://doi.org/10.1130/0091-7613\(1990\)018<0387:NDCFTI>2.3.CO;2](https://doi.org/10.1130/0091-7613(1990)018<0387:NDCFTI>2.3.CO;2).
- Veizer, J., 1983, Chemical diagenesis of carbonates: theory and application of trace element technique. In: Arthur, M.A., Anderson, T.F., Kaplan, I.R., Veizer, J., Land, L.S. (Eds.), *Stable Isotopes in Sedimentary Geology*, Vol. 10, Society of Economic Paleontologists and Mineralogists Short Course Notes, pp. III-1–III-100.
- Watanabe, K., Kanmera, K., Nakajima, K., 1979. Conodont biostratigraphy in the Kamura limestone (Triassic), Takachiho-cho, Nishiusuki-gun, Miyazaki Prefecture. In: Igo, H., Koike, T. (Eds.), *Biostratigraphy of Permian and Triassic Conodonts and Holothurian Sclerites in Japan*. Committee of Prof. M. Kanuma Retirement Ceremony, Tokyo, Japan, pp. 127–137.

- Wang, X., Planavsky, N. J., Reinhard, C. T., Hein, J. R., and Johnson, T. M., 2016, A Cenozoic seawater redox record derived from  $^{238}\text{U}/^{235}\text{U}$  in ferromanganese crusts: *American Journal of Science*, v. 316, no. 1, p. 64-83, doi: 10.2475/01.2016.02.
- Weyer, S., Anbar, A. D., Gerdes, A., Gordon, G. W., Algeo, T. J., and Boyle, E. A., 2008, Natural fractionation of  $^{238}\text{U}/^{235}\text{U}$ : *Geochimica et Cosmochimica Acta*, v. 72, no. 2, p. 345-359, doi: 10.1016/j.gca.2007.11.012.
- Zhang, L., Orchard, M. J., Algeo, T. J., Chen, Z.-Q., Lyu, Z., Zhao, L., Kaiho, K., Ma, B., and Liu, S., 2017, An intercalibrated Triassic conodont succession and carbonate carbon isotope profile, Kamura, Japan: *Palaeogeography, Palaeoclimatology, Palaeoecology*, in press, doi.org/10.1016/j.palaeo.2017.09.001.

## Supplementary figures

**Fig. DR1** Diagenetic plots. (A)  $\delta^{238}\text{U}$  profile, (B) Mn content profile, (C) Sr content profile, (D) Mn/Sr ratio profile, (E) Rb/Sr ratio profile, (F) U/Al ratio profile, (G) Mg/Ca molar ratio profile, and (H) Ce anomalies profile. The two green circles at the top of each records denote two outlier with high Mn/Sr ratios, and have been excluded in the discussion presented in the main text.

**Fig. DR2** Leaching results summary of  $\delta^{238}\text{U}$  and percent of U dissolved during each leaching step. Modern coral, SC-1, and SC-4 are three recent carbonate sediments that collected from the Bahamian carbonate platform. KAMD-20 and KAMD-31 are two Permian-Triassic aged carbonate sediments that collected from Kamura, Japan.

**Fig. DR3** Location of Japan, South China and Turkey at  $\sim 252$  Ma, the time of the end-Permian extinction (modified after Payne et al. (2007) ). (A): The Kamura section (Japan), this study. (B) The Dawen section (South China) studied by Brennecka et al. (2011). (C): The Dajiang section (South China) studied by Lau et al.(2016). (D): The Taşkent sections (Turkey) studied by Lau et al.(2016).

**Fig. DR4** A global compilation of  $\delta^{13}\text{C}$  data across the Permian-Triassic boundary.  $\delta^{13}\text{C}$  and conodont data of Kamura are from Zhang et al. (2017).  $\delta^{238}\text{U}$ ,  $\delta^{13}\text{C}$ , and conodont data of the Dawen section are from Brennecka et al. (2011) and Chen et al.(2009).  $\delta^{238}\text{U}$ ,  $\delta^{13}\text{C}$ , and conodont data of the Dajiang section and the Taşkent Section are from Lau et al.(2016). The well-characterized EMPE horizon and PTB horizon allow us to correlate these sections. The unit of the heights are in meters (m).

**Fig. DR5** Comparison of some common used diagenetic indicators among different Permian-Triassic sections. Data of the Kamura section are from this study. Data of the Dawen section are from Brennecka et al. (2011). Data of the Taşkent sections and the Dajiang section are from Lau et al.(2016). The empty spaces in the Dawen section denote that we have not found the related data from original publication.

**Fig. DR6** Comparison of cross-correlation between  $\delta^{238}\text{U}$  and some common used diagenetic indicators among different Permian-Triassic sections. Data of the Kamura section are from this study. Data of the Dawen section are from Brennecka et al. (2011). Data of the Taşkent sections and the Dajiang section are from Lau et al.(2016).

**Fig. DR7** Simplified schematic representation of the major source and sinks of U in the modern ocean along with their isotopic compositions (sources) or associated isotopic fractionations (sinks) [modified after Tissot and Dauphas (2015) and Wang et al. (2016)]. The  $\delta^{238}\text{U}$  of riverine input was from Andersen et al. (2016). In the alteration box, LT denotes low temperature alteration, and HT denotes high temperature alteration. Sinks including suboxic, carbonates, Mn-oxides, oceanic crust alteration, pelagic clays, and coastal retention are treated as one single "other" sink, with the fractionation factors being the weighted average of these individual sinks. All flux data (F) have a unit of  $10^6$  mol/yr.

**Fig. DR8** A LOWESS smoothing method estimate the possible timing of onset of anoxia. The timing is estimated based on the timing of onset of negative excursion in  $\delta^{238}\text{U}$  record. The red line denotes a LOWESS function smoothing of the combined data using a span of 0.2.

Fig. DR1

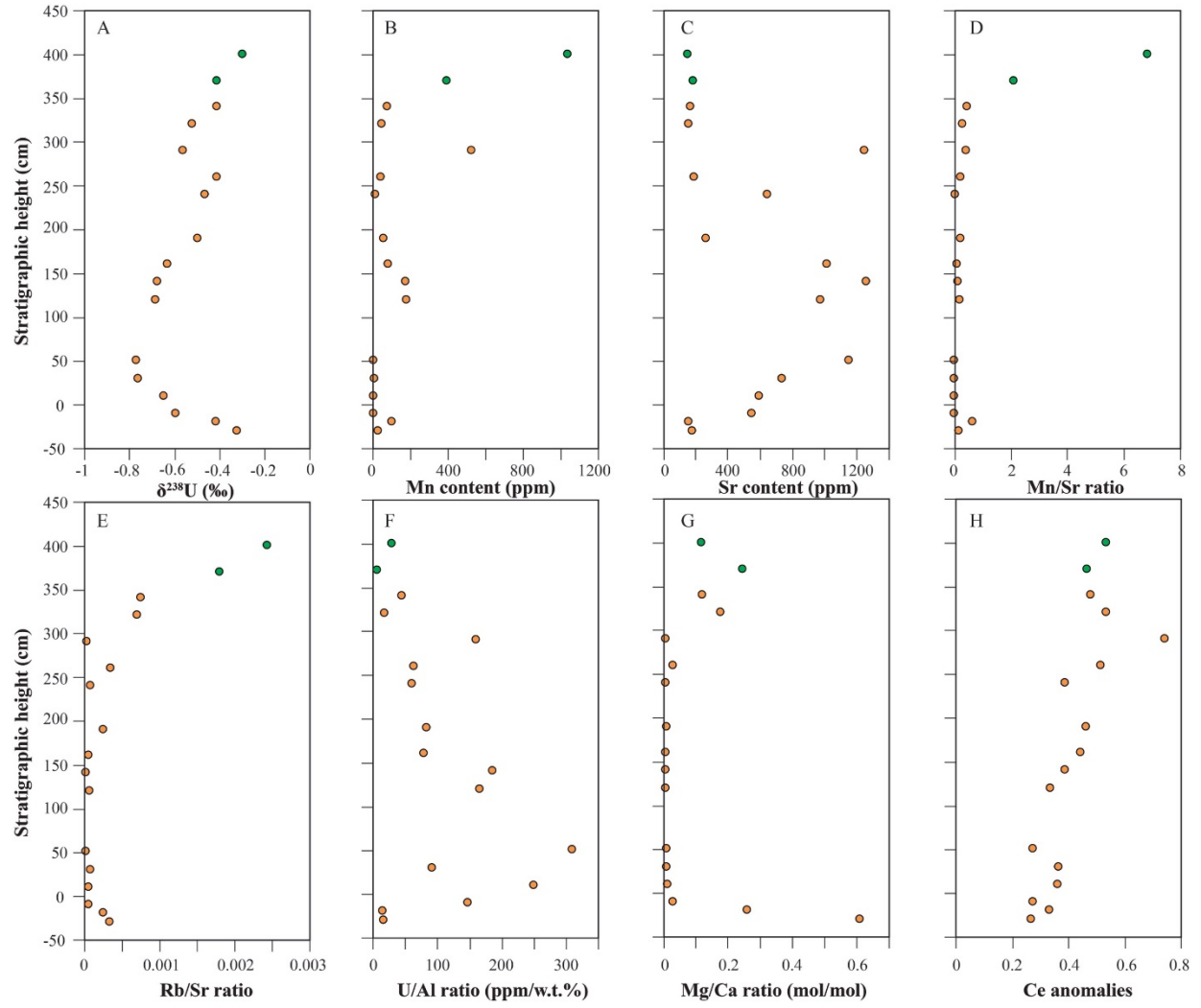


Fig. DR2

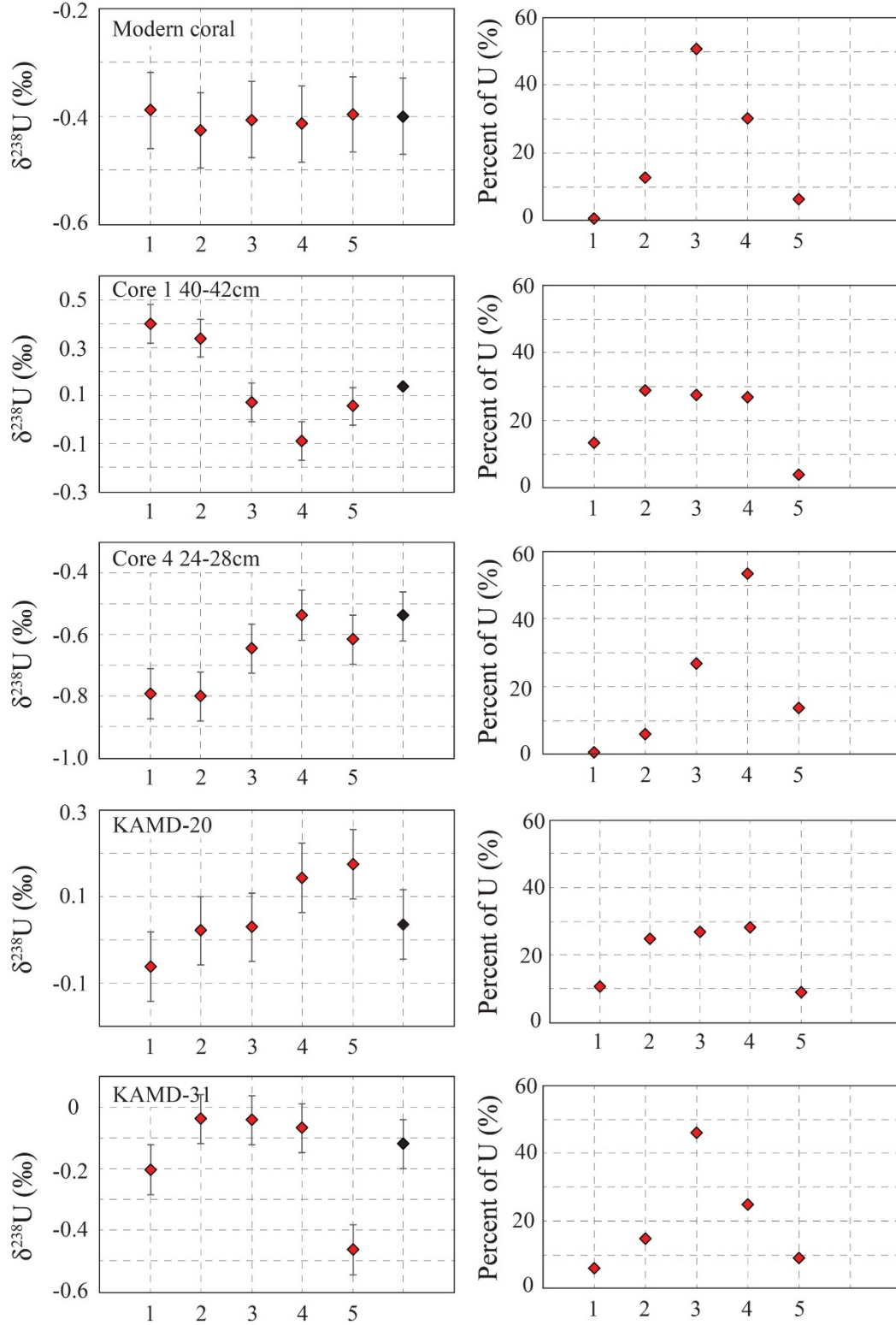


Fig. DR3

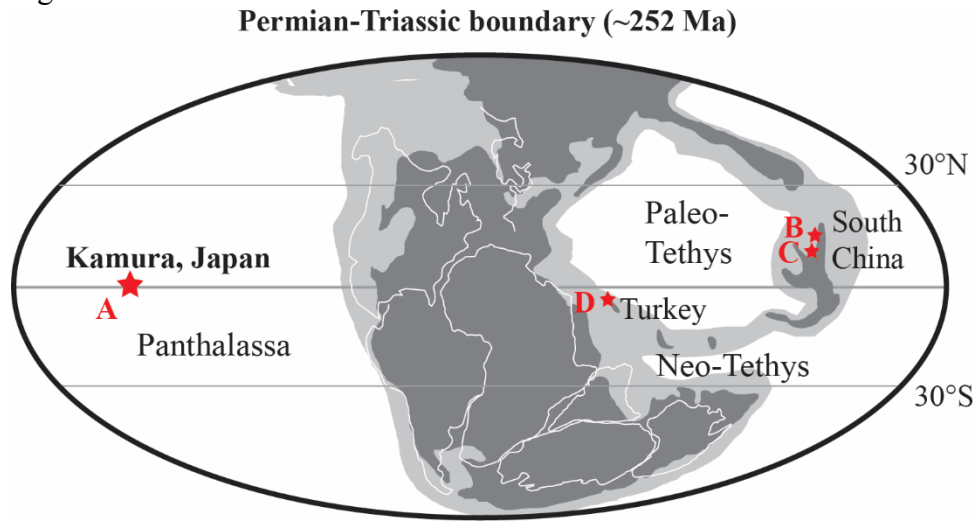


Fig. DR4

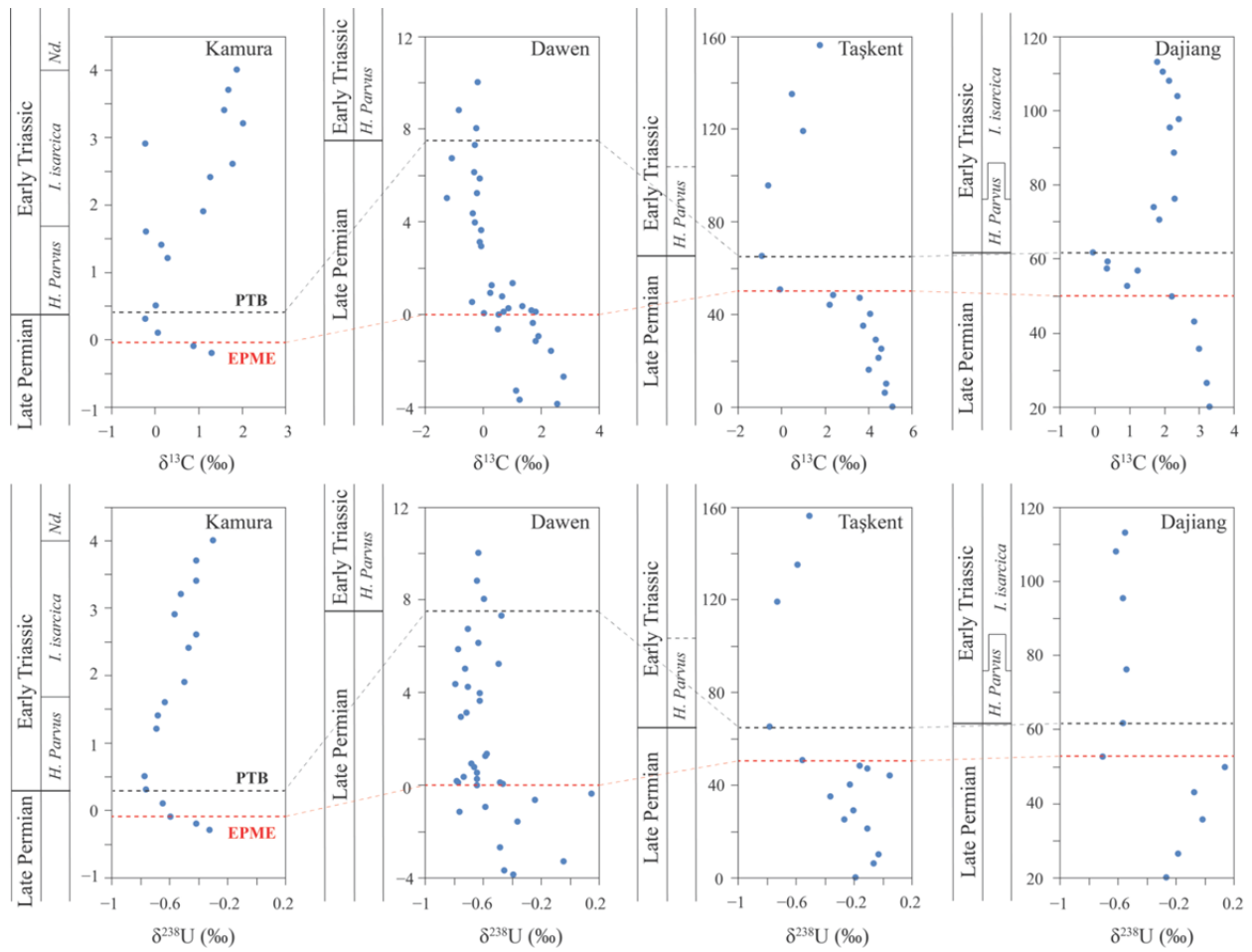


Fig. DR5

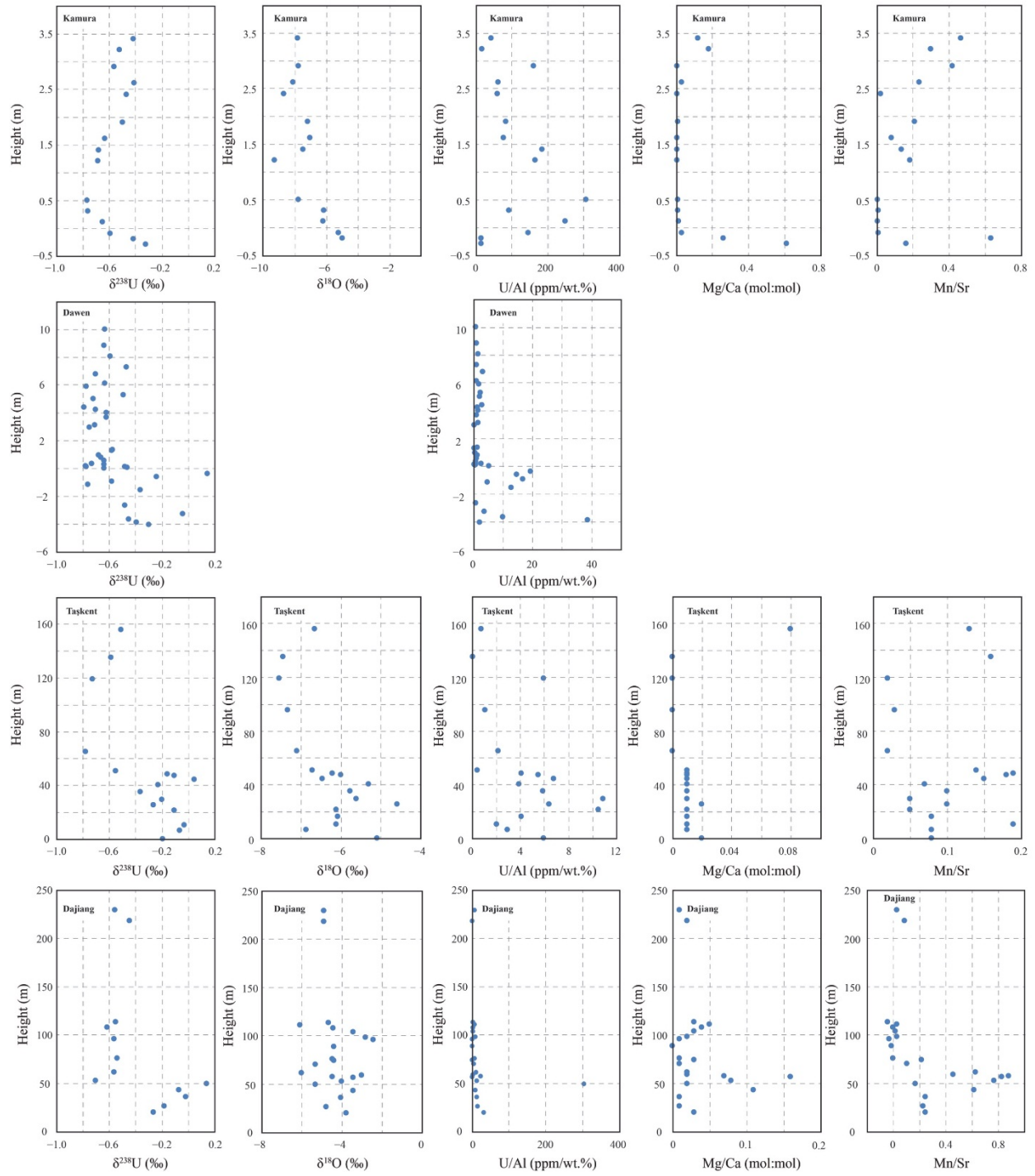


Fig. DR6

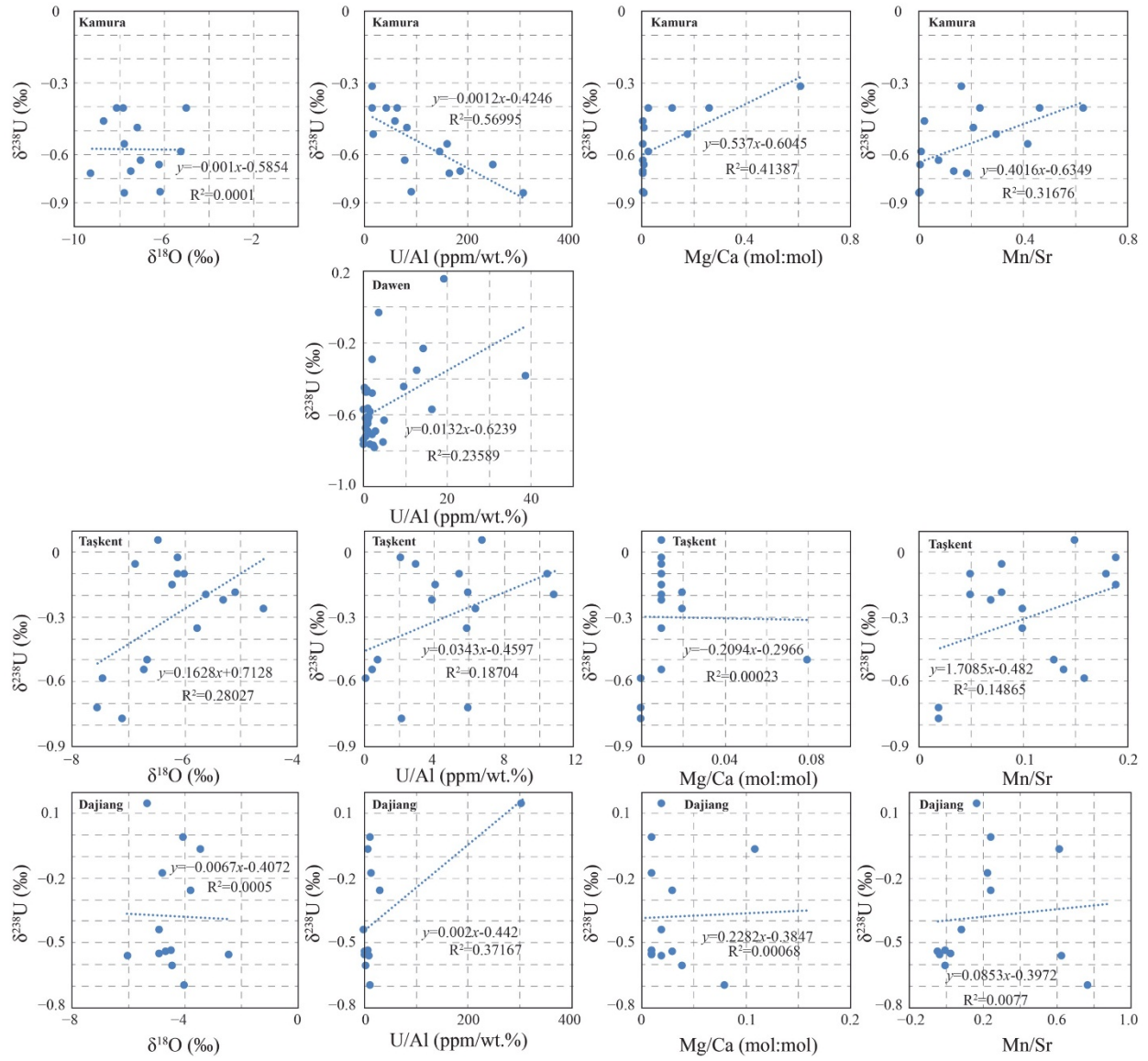


Fig. DR7

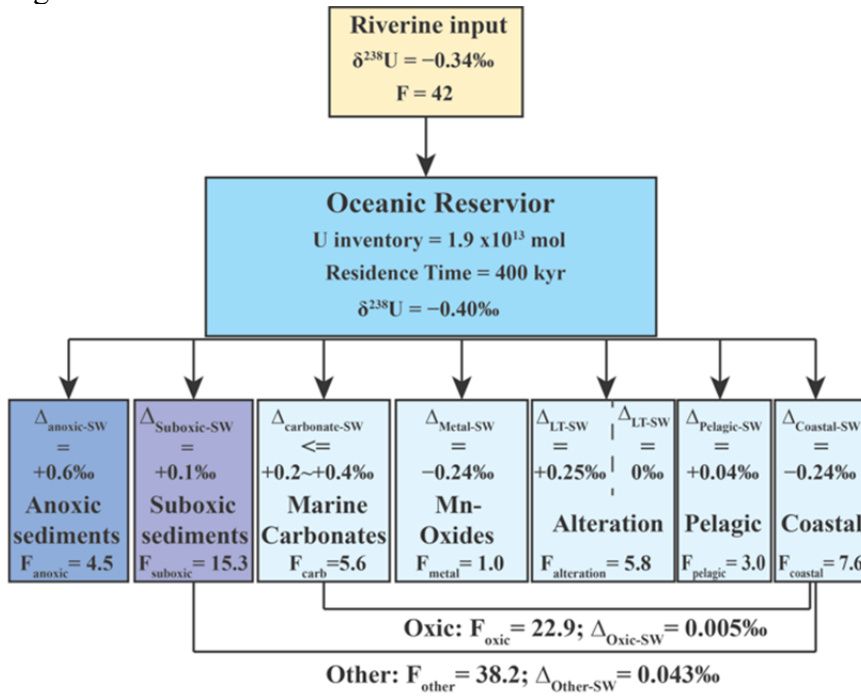


Fig. DR8

